PNAS RESEARCH ARTICLE | BIOPHYSICS AND COMPUTATIONAL BIOLOGY

Dimerization mechanism of an inverted-topology ion channel in membranes

Melanie Ernst[a], Esam A. Orabi[b], Randy B. Stockbridge[c], José D. Faraldo-Gómez[b,1], and Janice L. Robertson[a,1]

Edited by Karen G. Fleming, Johns Hopkins University, Baltimore, MD; received May 19, 2023; accepted September 28, 2023 by Editorial Board Member Nieng Yan

Many ion channels are multisubunit complexes where oligomerization is an obligatory requirement for function as the binding axis forms the charged permeation pathway. However, the mechanisms of in-membrane assembly of thermodynamically stable channels are largely unknown. Here, we demonstrate a key advance by reporting the dimerization equilibrium reaction of an inverted-topology, homodimeric fluoride channel Fluc in lipid bilayers. While the wild-type channel is a long-lived dimer, we leverage a known mutation, N43S, that weakens Na^+ binding in a buried site at the interface, thereby unlocking the complex for reversible association in lipid bilayers. Single-channel recordings show that Na^+ binding is required for fluoride conduction while single-molecule microscopy experiments demonstrate that N43S Fluc exists in a dynamic monomer–dimer equilibrium in the membrane, even following removal of Na^+. Quantifying the thermodynamic stability while titrating Na^+ indicates that dimerization occurs first, providing a membrane-embedded binding site where Na^+ binding weakly stabilizes the complex. To understand how these subunits form stable assemblies while presenting charged surfaces to the membrane, we carried out molecular dynamics simulations, which show the formation of a thinned membrane defect around the exposed dimerization interface. In simulations where subunits are permitted to encounter each other while preventing protein contacts, we observe spontaneous and selective association at the native interface, where stability is achieved by mitigation of the membrane defect. These results suggest a model wherein membrane-associated forces drive channel assembly in the native orientation while subsequent factors, such as Na^+ binding, result in channel activation.

ion channel | dimerization | single-molecule microscopy | Fluc | computational modeling

Significance

Ion channels are of critical importance in cellular physiology, where selective and properly timed permeation of ions across the membrane is a requirement for ionic homeostasis and excitability. Yet, we often do not understand what dictates proper folding and assembly of ion channels in membranes. Here, we present experimental measurements of the equilibrium assembly of an ion channel complex in membranes, a model system we developed based on the dual-topology fluoride ion channel Fluc, and report the linkage of the stability to buried sodium binding. Parallel computational studies demonstrate that the assembly of this species into dimers is driven by the membrane energetics alone, while sodium binding regulates the conductive state of the dimer.

Channels enable the high-throughput permeation of ions across the barrier of the cell membrane, oftentimes with exquisite chemical selectivity. To accomplish these tasks, a channel structure must feature a stable pathway for ion permeation offering chemical coordination and second-shell favorable electrostatic interactions, which together counter the otherwise prohibitive cost of traversing the low-dielectric core of the lipid bilayer. Despite significant architectural variability, many channel structures require the assembly of an oligomeric complex in the membrane where the ion conduction pathway is formed along the central axis. Examples include the voltage-gated potassium channels, transient receptor potential channels, and nicotinic acetylcholine receptors (1–4), among many other families.

The assembly of multimeric ion channels into functional units is therefore a reaction of essential importance in cellular physiology. Yet, the underlying molecular mechanisms remain poorly understood, as protein oligomerization reactions in membranes have been challenging to characterize. Fundamental insights have been gained in a few cases, however. Consider the channels formed by gramicidin peptides, which form continuous Na^+ selective pores upon dimerization. This involves two β-helix subunits, one in each bilayer leaflet (5), in a reversible process that is thermodynamically linked to environmental parameters such as the hydrophobic thickness of the surrounding membrane (6, 7). Aside from this model system, another integral membrane transport protein whose dimerization thermodynamics has been characterized is the CLC-ec1 Cl^-/H^+ antiporter, a homologue to voltage-gated chloride ion channels in humans. While the monomer is the functional unit, it has been shown to exist in a homodimerization equilibrium in membranes (8, 9), largely controlled by differentials in the lipid solvation energetics of the monomeric and dimeric states (10). Reversible oligomerization of membrane proteins occurs also beyond channel families; a remarkable example is the bacterial flagellar motor, whose membrane-embedded subunits have been shown to be in continuous exchange, even when the motor is active (11). Clearly, there is a growing body of evidence showing that many membrane proteins exist in a thermodynamic balance between pseudo-stable monomers

Author contributions: M.E., E.A.O., R.B.S., J.D.F.-G., and J.L.R. designed research; M.E., E.A.O., R.B.S., J.D.F.-G., and J.L.R. performed research; M.E., E.A.O., R.B.S., J.D.F.-G., and J.L.R. contributed new reagents/analytic tools; M.E., E.A.O., J.D.F.-G., and J.L.R. analyzed data; and M.E., E.A.O., R.B.S., J.D.F.-G., and J.L.R. wrote the paper.

The authors declare no competing interest.

This article is a PNAS Direct Submission. K.G.F. is a guest editor invited by the Editorial Board.

Copyright © 2023 the Author(s). Published by PNAS. This article is distributed under Creative Commons Attribution-NonCommercial-NoDerivatives License 4.0 (CC BY-NC-ND).

[1]To whom correspondence may be addressed. Email: jose.faraldo@nih.gov or janice.robertson@wustl.edu.

This article contains supporting information online at https://www.pnas.org/lookup/suppl/doi:10.1073/pnas.2308454120/-/DCSupplemental.

Published November 13, 2023.

and multimers, with both forms adapted to the hydrophobic environment of the membrane, though not identically. Nonetheless, what is particularly perplexing about oligomeric ion channels is that the monomeric form must expose charged ion-coordinating surfaces to the hydrophobic core of the lipid bilayer, implying that only the fully assembled oligomer state is viable in the membrane. This raises the question of whether ion channels can participate in thermodynamically defined equilibrium assembly reactions like the examples described above, even though the dissociated forms would perturb the hydrophobic core of the cellular membrane.

To begin to address this fundamental question, we developed a model system for studying ion channel subunit assembly in membranes based on the inverted-topology, homodimeric ion channel Fluc. The Fluc family consists of small, 4 transmembrane helix proteins that dimerize to form highly selective fluoride (F^-) channels. These proteins protect unicellular organisms from F^- accumulation in the cytoplasm, which inhibits enolase and pyrophosphatase, two enzymes essential for glycolytic metabolism and nucleic acid synthesis (12, 13). Flucs exhibit a remarkable $>10^4$-fold F^-/Cl^- selectivity and single-channel recordings show that they are almost always open, $P_{open,WT} > 95\%$ (14). Flucs are also the only channels discovered so far to adopt an inverted-topology dimer arrangement. While Flucs are small, the crystal structure of the *Bordetella pertussis* homologue (Fluc-Bpe) shows a large dimerization interface with a surface area per subunit of around 1,700 Å^2 (15, 16). Along the dimerization interface are two F^- permeation pathways with resolvable electronegative densities marking binding sites for F^- ions (17). In addition, there is an unusual electron density well removed from the F^- permeation pathways at the dimerization interface and at the very center of the lipid-bilayer core. The tetrahedral coordination formed by the backbones of G77 and T80 from each subunit indicates this density corresponds to a sodium ion (Na^+) residing along the protein's two-fold symmetry axis (Fig. 1*A*) (18). The unique location of Na^+ at the dimerization interface in the membrane core suggests that Na^+ binding to wild-type (WT) Fluc-Bpe locks the protein in the dimeric state. Indeed, Na^+ does not dissociate in WT Fluc-Bpe channels at ambient temperature (18). However, the mutation N43S weakens Na^+ binding by disrupting the hydrogen bonding network behind this central site, and introduces reversible Na^+ titration of F^- transport, as well as inhibition by Li^+ (18). This presents N43S Fluc-Bpe as a model system to examine the mechanism of ion channel assembly equilibrium in membranes.

Indeed, through a series of experimental and computational investigations, we report that the dimerization of N43S Fluc-Bpe in membranes follows a thermodynamic model where dissociated subunits exist in equilibrium with the dimer complex. Single-channel recordings show that N43S Fluc-Bpe remains an ion channel where the probability of channel opening, P_{open}, depends on Na^+. While Na^+ binding is required for channel activity, single-molecule photobleaching analysis reveals that it is not required for dimerization, indicating that the complex forms with strong affinity before Na^+ is bound. Since dimerization creates the Na^+ binding site, Na^+ is linked to the dimerization reaction, but binding, and therefore dimer stabilization, is weak. Coarse-grained (CG) molecular dynamics (MD) simulations of the Fluc-Bpe monomer in membranes show that the lipid bilayer forms a thinned and curved defect around the dimerization interface, like

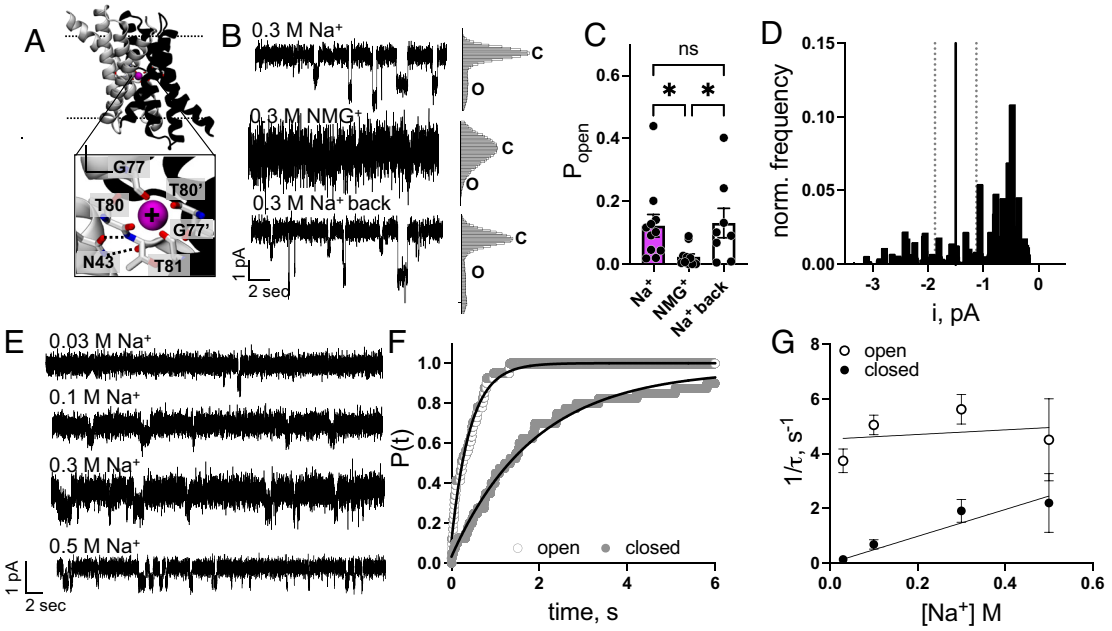

Fig. 1. Fluc N43S is a Na^+ gated ion channel. (*A*) Na^+ binding site in Fluc-Bpe (PDB ID: 5NKQ) with residues in coordination distance (G77, T80, G77′, T80′) to Na^+, N43 side chain which is within hydrogen bonding distance of backbone carbonyl group and backbone amide of T81. (*B*) Na^+ exchange in single channel recording. Representative trace of single channel recordings of N43S-Cy5 reconstituted at 0.05 μg/mg in *E. coli* polar lipids (EPL), inserted into a 2:1 1-palmitoyl-2-oleoyl-phosphatidylethanolamine (POPE)/1-palmitoyl-2-oleoyl-phosphatidylglycerol (POPG) bilayer and recorded at –200 mV. Opening of the channel is shown downward. Single channels were recorded in 300 mM NaF buffer in cis and trans chambers (Na^+). Then buffer was switched to 300 mM NMGF in a cis chamber (NMG). Buffer was then switched back to 300 mM NaF in a cis chamber (Na^+ back). Histograms on the *Right* of the traces show the current amplitude distribution of the trace. (*C*) Probability of channel opening calculated from 8 to 11 channels from two independent protein purifications. Data are reported as mean ± SE, n = 8 to 11. (*P*-values: Na^+ vs. NMG^+: 0.0293, NMG^+ vs. Na^+ back: 0.0296; Na^+ vs. Na^+ back: 0.8547, unpaired *t* test). (*D*) Open state current i) amplitude histogram of N43S-Cy5 channels recorded at –200 mV holding potential at 300 mM Na^+. Shown is the normalized frequency of the open states of 28 recorded channels from two independent protein purifications. The solid line marks the WT Fluc current amplitude, and the dotted line marks a 25% error (17). Zero current is defined as the mean level of the fully closed channel. (*E*) Single channel recordings with indicated concentrations of Na^+ with conditions as in *B*. (*F*) Cumulative distributions *P(t)* of closed (solid points) and open (open points) dwell times for a single N43S-Cy5 channel in the presence of 0.5 M Na^+. Solid lines show single-exponential fits. (*G*) Dependence of closed (solid points) and open (open points) time constants on [Na^+]. Each point represents mean ± SE time constant from 3-5 separate bilayers. Solid lines show fits to (Eqs. **5** and **6**) for closed and open intervals, respectively. $k_{on} = 4.9\ s^{-1}\ M^{-1}$ and $k_{off} = 4.5\ s^{-1}$.

that observed in our studies of CLC (10). Finally, simulations of freely diffusing monomers in the membrane, designed to preclude direct protein–protein contacts, nevertheless show that Fluc-Bpe selectively forms stable dimers in the native orientation, which selectively mitigate the membrane defect. Taken together, these studies demonstrate that the ion channel N43S Fluc-Bpe exists in a monomer–dimer equilibrium that appears to be strongly influenced by the morphological energetics of the membrane. We propose that this thermodynamic mechanism is shared by other ion channels and that it enables a cell to dynamically regulate ion channel assembly, function, and degradation through variations in composition and physical state of the lipid bilayer.

Results

N43S Fluc is a Na^+-Dependent Ion Channel. Previous structural studies of Fluc from two different homologues revealed a Na^+ bound at the center of the dimerization interface (15). This ion remains associated with the Fluc-Bpe channel throughout purification, indicating the structure of the dimer interface is highly stable (18). In proteoliposomes, elevated temperatures for extended times allow Na^+ to exchange with Li^+, but full removal of Na^+ results in precipitation (18). These observations suggest that passive dissociation of WT dimers in vitro will be rarely observed, and so WT Fluc-Bpe (henceforth called N43S) is impractical as a model system to study equilibrium assembly in membranes. Instead, we focused on N43S Fluc-Bpe (Fig. 1*A*), a mutant known to weaken Na^+ binding, reasoning that it would be conducive to spontaneous dimer dissociation. Before proceeding to investigate the dimerization of N43S, we sought to ascertain that this variant retains structural and functional features of the WT channel and is therefore a valid model system. N43S causes F^- efflux from proteoliposomes that depend on the Na^+ concentration (18), but intriguingly, it also limits the maximal efflux rate to about 2,660 ions per second at saturating Na^+ (18). This efflux rate is much smaller than that of WT Fluc-Bpe (henceforth called WT) [$\sim 10^7$ F^- ions/s at –200 mV (13)], and more aligned with those observed for secondary-active transporters, which generally involve complex conformational transitions resulting in rates of 100 to 10,000 ions per second, with an estimated theoretical limit of 100,000 (19, 20). This finding could be interpreted as indicative that N43S is structurally or mechanistically distinct from WT; however, it is also plausible that the mutation only influences Na^+ binding and that N43S functions as a channel, conducting fluoride ions at a rate comparable to WT, but with a lower open-state probability, P_{open}, explaining the slower macroscopic efflux.

To resolve this question conclusively, we carried out single-channel electrophysiological recordings of N43S Fluc reconstituted in *E. coli* polar lipids (EPL) fused into planar 2:1 POPE/POPG bilayers. Indeed, recordings of Cyanine-5 labeled N43S (N43S-Cy5) at saturating Na^+ (300 mM) showed single-channel activity (Fig. 1*B*), but with altered gating behavior. WT Fluc exhibits a $P_{open} > 0.95$ and a single-channel conductance of 5 pS with few closures or sub-conductance states (15, 17). However, at 300 mM Na^+, N43S-Cy5 Fluc is mostly nonconducting, exhibiting a $P_{open,Na} = 0.12 \pm 0.04$ (mean ± SE, n = 11) (Fig. 1*C*). Further, we observe a range of magnitudes, with the most observed population exhibiting ~2.5 pS (~ –0.5 pA at –200 mV), about half of the WT conductance (Fig. 1*D*). Independently, we find the channel gating is Na^+ dependent in a reversible manner (Fig. 1 *B* and *C* and *SI Appendix*, Fig. S1). After exchange of the cis chamber solution from 300 mM NaF to 300 mM n-methyl-d-glucamine (NMG)-F, the channel openings disappear, $P_{open,NMG} = 0.02 \pm 0.01$ (mean ± SE, n = 11), but return with the addition of 300 mM NaF buffer back to the chamber, with $P_{open,Na\text{-}back} = 0.13 \pm 0.05$ (mean ± SE, n = 8). The dependency of P_{open} on Na^+ is resolvable in the single-channel recordings (Fig. 1*E*), and dwell-time analysis of open and closed states show that they are exponentially distributed with time constants τ_o and τ_c, respectively (Fig. 1*F*). Plotting $1/\tau$ as a function of Na^+ concentration (Fig. 1*G*), we find that the open times are Na^+ independent, while the closures decrease with increasing Na^+, supporting a bimolecular binding scheme with Na^+ binding rate constants of $k_{on} = 4.9$ s^{-1} M^{-1} and $k_{off} = 4.5$ s^{-1}. These experiments demonstrate that N43S-Cy5 Fluc is a Na^+-dependent ion channel, and that the slow fluoride efflux rates are primarily explained by a decreased P_{open}, relative to WT Fluc, while the single-channel F^- conductance is more modestly affected indicating that WT and N43S dimers are structurally and mechanistically similar when Na^+ is bound.

N43S Fluc Exists in an Equilibrium Association Reaction where Dimerization Precedes Na^+ Binding. Having confirmed that N43S Fluc is an ion channel where P_{open} is Na^+ dependent, we then investigated whether the channel undergoes a dimerization reaction in the membrane. Specifically, we sought to examine whether dimerization and channel opening conferred by Na^+ binding are concurrent, like what is observed for gramicidin channels (6, 7). To examine this question, we measured the dimerization reaction of N43S-Cy5 Fluc in EPL bilayers following the removal of Na^+. Previous studies used a dialysis approach to remove Na^+ from proteoliposome samples in exchange with NMG (18). This method is effective, as evidenced by the loss of N43S-Cy5 function (*SI Appendix*, Fig. S2); however, we note that traces of Na^+ may remain as Na^+ is a major contaminant in many salts, and so we refer to this condition as "0" mM Na^+. To measure monomer–dimer equilibrium in membranes at "0" mM Na^+, we reconstituted N43S-Cy5 in EPL at protein densities ranging from $\chi = 1 \times 10^{-8}$ to 2×10^{-5} subunits/lipid and measured the photobleaching probability distributions using the subunit-capture approach (Fig. 2*A*) (8). This method recognizes that the photobleaching probability distribution follows Poisson statistics if one considers heterogenous compartments and multiple protein species, which can be modeled using a stochastic simulation approach (21). Single-molecule photobleaching analysis requires specific labeling of each subunit and knowledge of the labeling yield. Therefore, we spectrophotometrically measured the site-specific labeling of N43S Fluc at R128C with Cy5 via a thiol-maleimide reaction as well as the background labeling of the cysteine-less protein. We found $P_{site,N43S} = 0.67 \pm 0.01$ (mean ± SE, n = 23), with a nonspecific background labeling yield of $P_{bg} = 0.11 \pm 0.03$ (mean ± SE, n = 12) (*SI Appendix*, Fig. S3*A*).

Comparing the probability of single steps, P_1, of N43S-Cy5 to the simulated monomer, *M*, and dimer, *D*, species, we observed that the protein population shifts from dissociated subunits to associated dimers as a function of the protein density in the membrane, indicative of an equilibrium dimerization reaction (Fig. 2*B*). If this system truly is in a dynamic equilibrium, then a perturbation by dilution will also yield a shift in the photobleaching probability distribution in the monomeric direction. In lipid bilayers, dilution is not spontaneous, but can be achieved via freeze/thaw fusion of proteoliposome samples with excess membrane. As we dilute N43S-Cy5 Fluc at $\chi = 2 \times 10^{-5}$ subunits/lipid with 20 times excess membrane we observe an increase in P_1 of the freeze/thawed sample, which converges with P_1 values for a sample that was directly reconstituted at $\chi = 1 \times 10^{-6}$ subunits/lipid, demonstrating path-independence of the dimer signal (Fig. 2*C*). As these experiments report only on subunit dissociation, we also assessed the formation of new dimers after subunit exchange. We find that

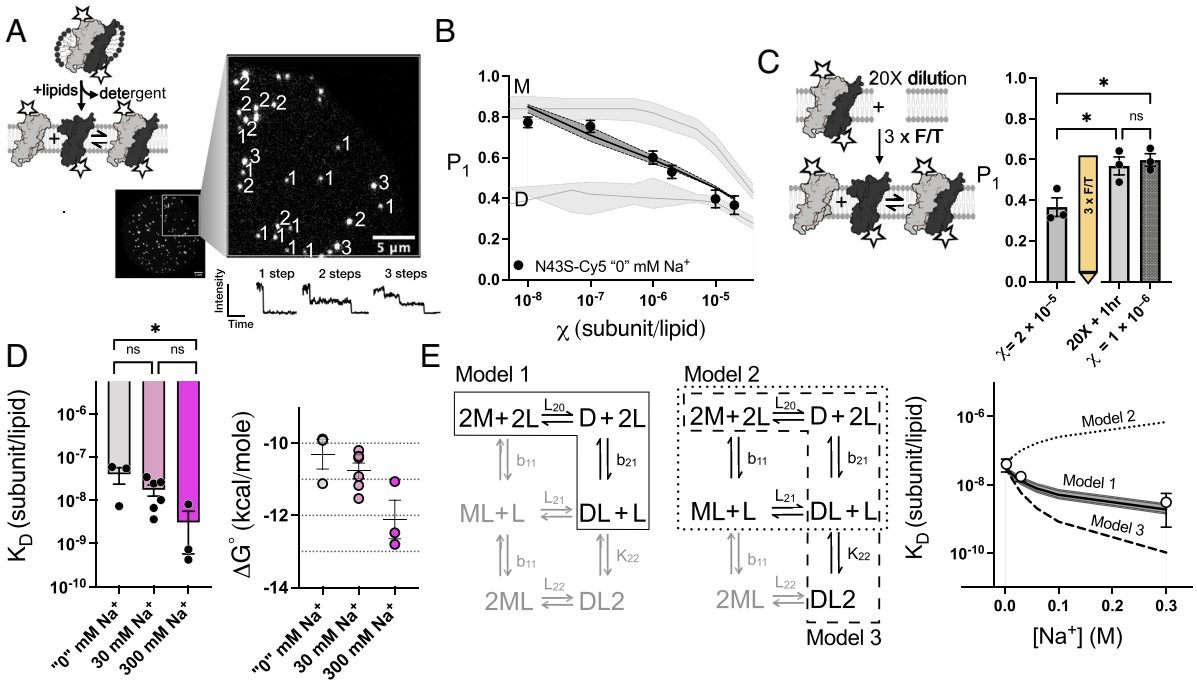

Fig. 2. N43S-Cy5 Fluc forms stable dimers without Na^+ but provides a single Na^+ binding site. (*A*) Cartoon representation of reconstituting Cyanine5-labeled Fluc N43S (N43S-Cy5) into EPL bilayers and photobleaching analysis after subunit capture as described by ref. 8. Liposomes are imaged under the TIRF microscope and photobleaching steps are counted. (*B*) N43S-Cy5 shows a shift in monomer–dimer distribution over $\chi = 1 \times 10^{-8}$ subunit/lipid to $\chi = 2 \times 10^{-5}$ subunit/lipid. χ is the observed mole fraction considering protein recovery yield = 2. Photobleaching probabilities of a single step (P_1) vs. χ for N43S-Cy5 and simulated monomer, *M*, and dimer, *D*, controls. The solid line represents the mean ± σ of the global fit to the experimental data fitted using (22). Data are reported as mean ± SE, n = 3. (*C*) Dilution of reconstituted protein with excess membrane shows a shift in the photobleaching probability distribution. N43S-Cy5 reconstituted at $\chi = 2 \times 10^{-5}$ was diluted by 3× F/T fusion with 20X excess membrane and incubated at room temperature for 1 h. $\chi = 1 \times 10^{-6}$ subunit/lipid shows the P_1 for the reconstituted sample. All data are reported as mean ± SE, n = 3 (*P*-values: $\chi = 2 \times 10^{-5}$ vs. 20× + 1 h: 0.0474, $\chi = 2 \times 10^{-5}$ vs. $\chi = 1 \times 10^{-6}$: 0.0270; 20× +1 h vs. $\chi = 1 \times 10^{-6}$: 0.9554, ordinary one-way ANOVA). (*D*) Fluc-N43S dimer is stabilized with increasing concentrations of Na^+. Fitted K_D following (23) and calculated $\Delta G°$ for "0" mM Na^+, 30 mM Na^+, 300 mM Na^+. Data are reported as mean ± SE, n = 3 to 6 (*P*-values: "0" mM Na^+ vs. 30 mM Na^+: 0.0840, 30 mM Na^+ vs. 300 mM Na^+: 0.2451, "0" mM Na^+ vs. 300 mM Na^+: 0.0222, ordinary one-way ANOVA). (*E*) Reaction species array for monomer–dimer reaction with single-site binding of the ligand (*L*) to each monomer subunit (*M*) adapted from ref. 24. Equilibrium constants beside the arrows apply to those reactions. The reaction between dimer (*D*) and *2L* to form D_2L_2 is described by the equilibrium constant $b_{22} = b_{21}K_{22}$. Sub-reactions of models are indicated with lines. Model 1 (solid line) does not consider b_{11}, or K_{22}; Model 2 (dotted line) does not consider K_{22}; Model 3 (dashed line) does not consider b_{11}. Na^+ binding can be described with a single binding site to the dimer model (Model 1, solid line). Fitted K_D vs. Na^+ concentration as well as best fit using Model 1 (solid line, $L_{20} = 2.8 \pm 0.3 \times 10^7$ lipid/subunit, $b_{21} = 60.4 \pm 9.6\ M^{-1}$ mean ± SD) and simulated data for the single binding site to the monomer and dimer with equal affinities (Model 2, dotted line) as well as a two independent binding sites to the dimer (Model 3, dashed line). Data were fitted using Scientist® and the models were created using MATLAB®.

N43S Fluc dimers labelled with donor and acceptor fluorophores readily exchange subunits monitored by the increase in the Förster Resonance Energy Transfer (FRET) signal (*SI Appendix*, Fig. S3 *B–G*), as has been observed for CLC-ec1 (9).

Having verified that N43S Fluc is in a dynamic monomer–dimer equilibrium, we proceeded to quantify the thermodynamic stability of the N43S-Cy5 dimer, based on the observed photobleaching probability distributions (Fig. 2*B* and *SI Appendix*, Fig. S4*A*). To do this, we used a stochastic simulation of the Poisson process of protein reconstitution into liposomes, with which we modeled the expected photobleaching probability distribution for a reactive monomer–dimer system at a given condition (8). Given that site-specific and nonspecific background fluorophore labeling yields are known (P_{fluor}, P_{bg}) we can carry out an iterative search of the dimerization dissociation constant K_D that best-fits the experimental photobleaching probability data (P_1, P_2, P_{3+}) (22). Additionally, we used the cryo-electron microscopy liposome size distribution (25), and measured the subunit/lipid mole fraction after reconstitution, freeze/thaw, and extrusion, which shows that the experimental mole fraction is 200% of that originally reconstituted (*SI Appendix*, Fig. S4*B*). This increase results from a significant loss in lipids (~ 50%) while the protein recovery is ~100% (*SI Appendix*, Fig. S4*B*). Using the values of $P_{fluor} = 0.67$ and $P_{bg} = 0.11$, we find the best-fit model yields $K_D = 4.0 \pm 1.6 \times 10^{-8}$ subunits/lipid (mean ± SE, n = 3), corresponding to $\Delta G° = -10.3 \pm 0.4$ kcal/mole, 1 subunit/lipid standard state (Fig. 2*B* and *SI Appendix*, Fig. S4*A*). This demonstrates that N43S Fluc forms dimers even upon removal of Na^+, with a thermodynamic stability that is comparable to what was reported for CLC-ec1 I422W (8, 26). In contrast, we did not observe an equilibrium reaction for WT Fluc under our current conditions (*SI Appendix*, Figs. S5 and S6).

Having established that N43S Fluc exists in a dimerization equilibrium in membranes upon removal of Na^+, we investigated whether Na^+ is a stabilizing factor for Fluc dimerization. Increasing Na^+ does affect dimerization but the contribution is a small fraction of the total free energy, stabilizing the complex by $\Delta\Delta G = 1.8$ kcal/mole as Na^+ is raised to 300 mM (Fig. 2*D* and *SI Appendix*, Table S1). We find that our experimental data agree well with a linked reaction model in which two monomers first associate into a dimer complex, followed by Na^+ binding (Fig. 2*E*) and we estimate the Na^+ binding constant $K_{D,Na+} = 1/b_{21} = 16.6 \pm 2.7$ mM (mean ± SD; Fig. 2*E* and *SI Appendix*, Table S1). This also allows us to extrapolate the dimer stability to the absence of Na^+ yielding $K_{eq} = 2.8 \pm 0.3 \times 10^7$ lipid/subunit (mean ± SD, n = 3), corresponding to $\Delta G° = -10.2 \pm 0.9$ kcal/mole, 1 subunit/lipid standard state, comparable to the "0" mM Na^+ measurement. This data is also comparable to previous functional studies obtaining $K_{D,Na+}$ = 3.6 mM from fitting Fluc-mediated fluoride transport of N43S to Na^+ with a single binding site association reaction (18). In contrast, the experimental data do not agree with the alternative

case in which a Na^+ ion binds to each monomer (Model 2) or a model in which two Na^+ can bind to the dimer (Model 3) (Fig. 2*E* and *SI Appendix*, Table S1). Together, our comparison of different hypothetical reaction schemes supports a model where Na^+ linkage to the dimerization reaction occurs via a single Na^+ binding site to the preformed dimer state (*SI Appendix*, Fig. S7). We note that the binding site exhibits size specificity as we observe binding of Li^+ but not larger cations such as K^+ (*SI Appendix*, Fig. S8), however, the channel is only functional when bound to Na^+.

Fluc Dimerization is Coupled to Membrane Morphology Energetics. Our experiments demonstrate that N43S Fluc forms stable dimers in membranes, and that this occurs before Na^+ binding, i.e., prior to the formation of the tight complex captured in crystal structures of the fluoride-bound Fluc dimer. This observation implies that there is a driving force that sustains a metastable encounter complex of Fluc monomers in the membrane, sufficiently long-lived to permit Na^+ binding and thereby activate the channel. The morphology of the bilayer around specific structural states can differ based on the protein–lipid interface and these morphological changes might contribute to the thermodynamic and kinetic stability of these states, favoring or disfavoring certain states over others (27). To investigate whether the membrane morphology of the surrounding bilayer differs for the monomeric vs. dimeric state, we carried out CG MD simulations of monomeric and dimeric Fluc-Bpe in POPE/POPG membranes. The calculated trajectories are 50 μs long, which allows for complete mixing of the two lipid species as well as multiple turnovers of all lipid molecules in the protein solvation shells in exchange for other lipids in the bulk (10). Inspection of the membrane morphology in these trajectories, through 2D maps of the hydrophobic thickness, shows the monomer induces a thinned-membrane defect at the exposed dimerization interface which disappears upon complete dimerization (Fig. 3*A*). It is worth noting that the defect induced by the monomer can be observed for both the WT protein and the N43S mutant, and both in CG and all-atom MD simulations (*SI Appendix*, Fig. S9). 3D density maps further reveal that this deformation develops to allow hydration of the exposed charged/polar residues that ultimately form the Na^+ binding site as well as additional surrounding residues (Fig. 3*B*). Interestingly, each monomer introduces an asymmetric deformation with respect to the membrane plane. The defect is oriented and isolated to a single leaflet, with the other subunit, in an inverted topology, providing a defect on the other leaflet. While thinning is accompanied by an increase in chain compression (Fig. 3*C*), these changes are minimal, less than 1 Å and smaller than the length of the C-C bond. Instead, the major change in thickness is attributed to lipid tilting (Fig. 3*D*) and increased entanglement between the two leaflets (Fig. 3*E*). These defects are entirely absent for the dimer. Thus, while the protein surface appears to be suitably solvated for both monomer and dimer, adequate solvation of the monomer requires a significant

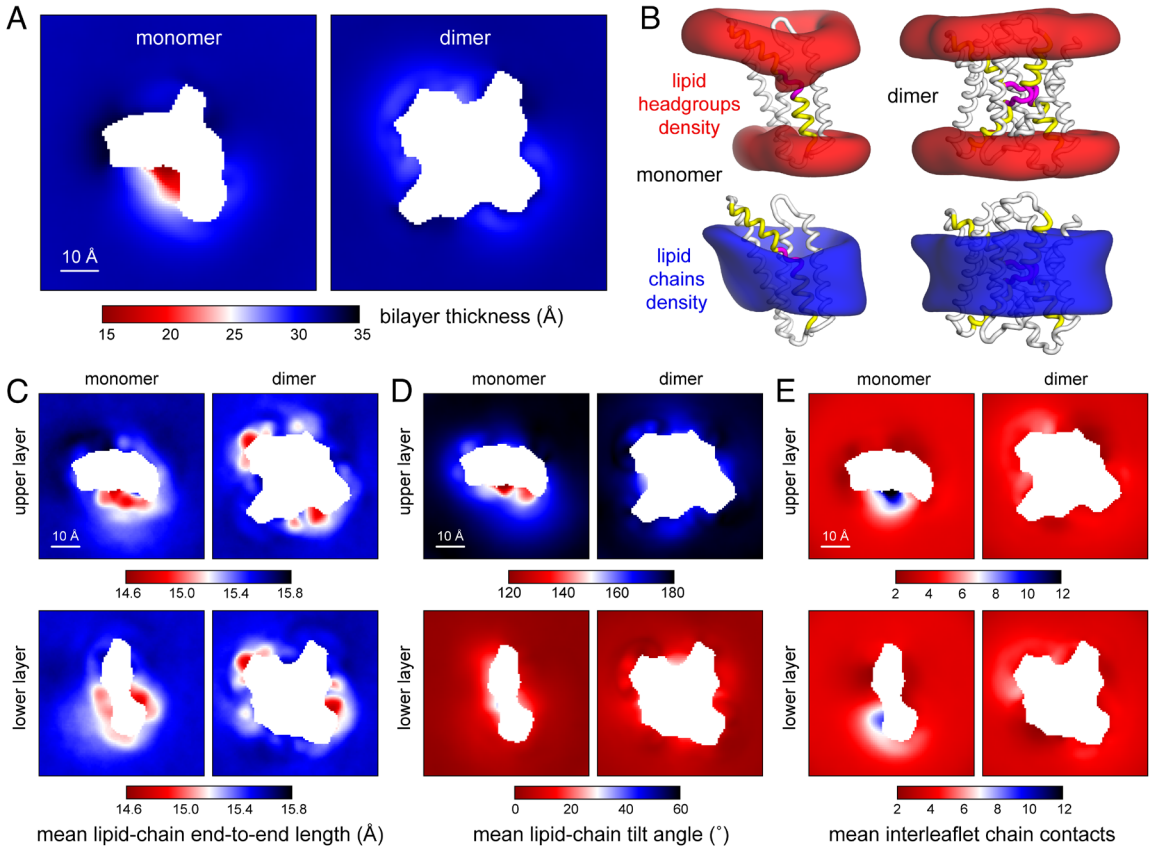

Fig. 3. Membrane morphology around Fluc monomer and dimer from MD simulations. Results are shown for 50 μs trajectories of either state in POPE/POPG membranes, analyzed using MOSAICS (28). All simulations are based on the CG MARTINI force field. (*A*) 2D map of the local bilayer thickness, quantified by the separation between ester layers in either leaflet. The thinned defect in the monomer marks the location of the dimerization interface. See also *SI Appendix*, Fig. S9 for simulations of monomeric N43S mutant, using both CG and all-atom representations. (*B*) 3D density maps for the head-groups (red) or acyl chains (blue) in the vicinity (10 Å) of the protein (white cartoon) for monomer and dimer. The dimerization interface is indicated in yellow, and the Na^+ binding site in magenta. 2D maps of (*C*) mean lipid-chain end-to-end length, (*D*) mean lipid-chain tilt angle relative to the bilayer perpendicular (angle is calculated between the vector defined by the ester to acyl-chain and membrane normal, pointing up, such that bulk lipids have an angle of 180° in the upper leaflet and 0° in the lower layer), and (*E*) mean number of leaflet-leaflet contacts, for both the upper and lower leaflets of the bilayer.

nonbilayer defect, i.e., an energetic penalty in the dissociated state. We thus reasoned that this membrane-dependent energetic penalty is what stabilizes the encounter complex of Fluc monomers prior to formation of the active dimer form.

To test this hypothesis, we carried out a second set of simulations wherein two Fluc-Bpe monomers in inverted orientations were positioned at least 5 nm away from each other, in four different starting configurations; each system was then equilibrated and simulated for 30 μs. To specifically examine the mediating role of the membrane, we introduced a short-range repulsive force between the two monomers, which effectively precludes the formation of a contact protein–protein interface. In other words, while the monomers are free to diffuse and transiently collide, they are not permitted to form direct protein–protein interactions in any orientation, an approach that also enabled us to avoid known deficiencies in the CG representation of this kind of interactions (29). Over the course of the trajectories, we observed multiple reversible collisions between monomers in nonnative orientations (Fig. 4*A*). However, when the two monomers happened to approach each other oriented as in the native dimer, i.e., in a manner that aligns the corresponding membrane defects, the monomers formed a noncontact dimer that was stable for the remainder of the simulation. This behavior was reproducible and observed in all replicate simulations. Time-averaged analysis of the lipid configurations in the monomer, noncontact dimer, and dimer states reveals the changes in lipid solvation accompanied with association (Fig. 4*B*). While the monomer carries a nonbilayer defect, exhibiting tilted and entangled lipids, the noncontact dimer allows the head-groups to fan out into a toroidal geometry that appears to match the polar/charged features of the Fluc dimerization interfaces (Fig. 4*C*), and is therefore advantageous. Ultimately, full dimerization requires expulsion of all these lipids, where they can return to their preferred bilayer state (Fig. 4*D*). Altogether, these results demonstrate that differences in membrane morphology and solvation energetics can physically drive Fluc

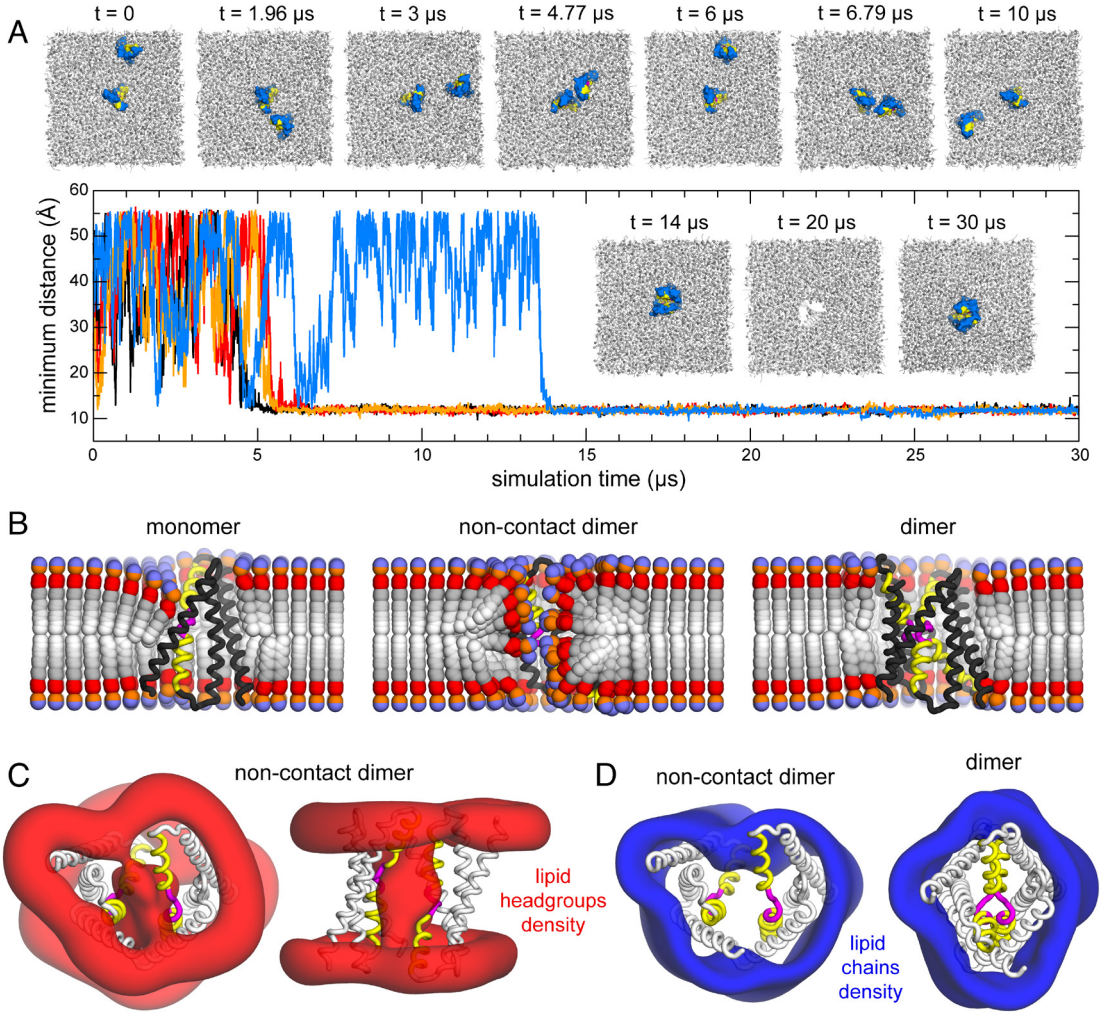

Fig. 4. Fluc dimerization is coupled to membrane morphology energetics. Results are shown for four independent trajectories of 30 μs in POPE/POPG membranes, analyzed using MOSAICS (28). All simulations are based on the CG MARTINI force field. (*A*) When freely diffusing Fluc monomers (marine blue) encounter each other in an orientation that aligns their dimerization interface (yellow) and Na^+ binding motifs (magenta), they form a lipid-mediated encounter complex, stable even in the absence of protein–protein contacts (which are excluded by design). Other orientations are unstable. Snapshots are shown of one of the trajectories at various time points (*t*), with the protein hidden in the 20 μs snapshot to highlight the layer of lipids that remain between the two subunits. Shown is also the minimum distance between monomers (measured at their backbones) vs. simulation time, for each of the 4 independent trajectories, showing the same noncontact complex is ultimately observed in all cases. (*B*) Time averages of the instantaneous 3D conformation of lipid molecules residing in different positions across the membrane plane. Acyl chains (grayscale), ester linkages (red), and head-groups (orange/purple) are shown as spheres. Note perfectly isotropic dynamics, when time averaged, results in a linear structure for the entire molecule, perpendicular to the membrane mid-plane, and with both acyl chains superposed. These structures are therefore nonphysical, but they reveal the mean tilt of the lipid molecules across the membrane as well as the degree of contacts between leaflets. Data is shown for the monomer, for the noncontact dimer (from simulations described in *A*), and for the dimer. (*C*) 3D density maps for the lipid headgroups (red) in the vicinity (10 Å) of the protein (white cartoon) for the noncontact dimer. (*D*) 3D density maps for the acyl chains (blue) in the vicinity (10 Å) of the protein (white cartoon) for the noncontact dimer and for the fully assembled dimer.

monomers into a noncontact dimer with the native orientation, prior to Na^+ binding and the formation of a tight protein–protein interface suitable for F^- permeation.

Discussion

α-Helical Ion Channel Subunits Can Exist in a Balance of Dissociated and Associated States Supporting a Thermodynamic Model of Assembly in Membranes. Our investigation demonstrates that an obligate homomeric ion channel can exist in a monomer–dimer equilibrium in membranes. For Fluc, this becomes apparent once we destabilize the central Na^+ binding site via the N43S mutation. While this mutation reduces the macroscopic fluoride permeation rate to a value reminiscent of a secondary-active transporter, our electrophysiological measurements demonstrate that N43S Fluc is a de facto channel whose single-channel conductance is within twofold of the WT protein. We therefore conclude that WT and N43S dimers are structurally and mechanistically similar when Na^+ is bound. For N43S, however, the probability of channel opening is strictly coupled to the Na^+ concentration. This indicates that N43S Fluc dimers must be conformationally flexible to allow for equilibrium titration of Na^+, since the ion binds to a site at the core of the dimerization interface (15). Indeed, our results for N43S Fluc demonstrate that the removal of Na^+ is not concurrent with dissociation into monomers, as our single-molecule photobleaching studies demonstrate that the protein dimerizes, and in fact forms stable complexes with a K_{eq} = 2.8 ± 0.3 × 10^7 subunits/lipid, corresponding to $\Delta G°$ = −10.2 ± 0.9 kcal/mole, 1 subunit/lipid standard state, when extrapolating to the condition where Na^+ is absent. To relate this to a biological reference, assuming an inner membrane surface area of 4 μm^2 containing ~10^7 lipids, this means that if just two N43S Fluc subunits are expressed in an *E. coli* cell then these subunits would be observed as dimers 70% of the time. It is reasonable to expect that more than two protein copies would be expressed upon activation of the fluoride riboswitch (30) and so we predict that a construct such as N43S would be dimeric in the cellular environment. At 300 mM Na^+, closer to biological salt conditions, the dimerization would be further stabilized, by an additional 1.8 kcal/mole.

Together, these factors present the possibility that Fluc monomers may be independently expressed in the membrane, released, and then form stable, but dynamic dimer complexes that exist in a thermodynamic balance. It is still an open question whether dynamic assembly like this is generalizable to other channels, or even to WT Fluc for that matter, but the same dynamic behavior has been observed for dimers of the CLC-ec1 chloride/proton antiporter (8, 9) and high-speed atomic force microscopy imaging show the assembly of TRPV3 channel complexes in real time (31). Altogether, these results present the possibility that dynamic association and dissociation of ion channels could exist in cellular membranes, highlighting an additional mechanism for modulating protein activity alongside direct regulation of the assembled form. In this case, changes in the reaction parameters, e.g., the global or local protein density, or lipoidal solvent composition, could shift the reaction equilibrium and decrease the number of assembled and activatable channels in the membrane. In addition, the dissociated form could then be linked to mechanisms of degradation (32). Further studies are required to understand if this occurs at a biologically meaningful level, but our results demonstrate that these reactions are physically possible.

Fluc Dimerization Eliminates Costly Lipid-Bilayer Defects, An Emerging Theme for Membrane Protein Oligomerization. The observation that N43S Fluc exists in a monomer–dimer equilibrium in membranes, whereby stable but conformationally flexible dimers are formed in the absence of Na^+, raises the question of what thermodynamic forces sustain this association. To understand this process, we first considered the dissociated Fluc monomer in the membrane. In this state, 1,700 $Å^2$ of previously buried surface area per monomer becomes exposed to the surrounding lipid and water solvent (15), including polar and charged motifs that would otherwise interact with F^- or Na^+. Since exposure of these motifs to the low-dielectric membrane core is electrostatically unfavorable, the surrounding membrane changes its shape to minimize hydrophobic mismatch (*SI Appendix*, Fig. S9). Our MD simulations show that the membrane morphology becomes nonbilayer like, with lipids significantly tilted to facilitate access to hydration. While polar and charged motifs on the protein are now more adequately solvated, this state incurs an energetic strain on the lipid bilayer. From recent studies, we know that the morphological energetics of the membrane are nonnegligible and must therefore be incorporated into the conceptual models and theories used to describe membrane-protein reaction mechanisms (27). Indeed, our simulations of free Fluc subunits, that explore all configurations where protein contacts cannot form, demonstrates that dimerization is overwhelmingly favorable, but only at the native interface. This result demonstrates that it is the membrane energetics, and the relief of the thinned, nonbilayer defect, that drives Fluc to ultimately dimerize in this configuration. This is like our findings for CLC dimerization, which bind via a hydrophobic interface that also introduces a thinned, nonbilayer defect in the monomeric state (10). Thus, the observation that both Fluc, via a polar/charged interface and CLC, via a greasy interface, have affinity due to their differential membrane structures, presents the membrane as a generalizable driving force for specific, oriented membrane protein assembly in membranes. Note, in Fluc, this stable state does not correspond to the presumed final, functional state, which we assume corresponds to the crystal structures (15, 17). This noncontact dimer or encounter complex is mediated by lipid head-groups but is more energetically stable in the membrane than the dissociated monomers and their thinned defect. Therefore, we propose that it is a lipid-solvated stable intermediate along the dimer pathway stabilized by the membrane. Of course, the protein plays a role also, but it is to adopt a stable monomeric structure that imposes a change in the surrounding membrane structure as well as providing precise chemical interactions to form the fluoride selective pore. We note that these types of lipid-solvated noncontact complexes have been observed previously, notably with the adenosine triphosphate (ATP) synthase, that dimerizes at a distance to stabilize a bent structure of the membrane, promoting self-assembly in rows along the cristae of mitochondria (33).

Assembly Via a Noncontact Dimer State Provides a Path for Na^+ Binding. The observation of a noncontact lipid-solvated state allows us to speculate about the mechanism of Na^+ binding to Fluc channels. Previously, it had been demonstrated that WT Fluc possesses a buried Na^+ that does not dissociate, unless the protein is heated for an extended time (18). Naturally, this raises the question of how Na^+ accesses its binding site in the first place. One possibility is that the N43S mutation promotes a local conformational change that provides access to the Na^+ binding site. However, we consider such structural rearrangements unlikely as the channel is formed by two, identical but inverted subunits that would be capable of making the same rearrangements on both sides, thus making it permeable to Na^+, which is not observed experimentally (18). Therefore, based on our findings, we propose that when N43S Fluc subunits are expressed in the cellular membrane, they fold into metastable monomeric structures that ultimately associate into dimers, to eliminate the unfavorable thermodynamic cost of lipid solvation of the dissociated state.

Dimerization proceeds via the formation of a noncontact lipid-solvated stable intermediate where water and Na^+ can penetrate the head-group region between the two subunits, but without a continuous pathway across the membrane (*SI Appendix*, Fig. S7). With this, the site, formed by the protein backbone, becomes stabilized and assembles around the Na^+ ion, expelling lipids in the last step to allow for the two subunits to come together in the state that permits highly selective F^- permeation. Our studies of the equilibrium linkage of Na^+, or even Li^+ binding to dimerization, support the model that a binding site is present only in the dimer state. The linkage of Na^+ and Li^+ binding to dimer stability is weak in N43S Fluc, and therefore indicates that the ion binding is not a major driving force for dimerization. However, Na^+ is absolutely required for channel activation, meaning that Na^+ stabilizes the conductive structure upon binding. Interestingly, Li^+ presents the same weakly stabilizing effect on dimerization, but inhibits channel function, indicating that it binds but does not stabilize the proper conformation of the channel that allows for F^- permeation.

Extrapolations to the WT Fluc Assembly Reaction. The studies that we present here are on a mutant form of Fluc, N43S, that enables Na^+ binding and subunit exchange in a dynamic manner. However, this is not the biological form of the protein, and WT Fluc does not exhibit any evidence of a dynamic equilibrium. Fusion of WT-Cy3 and WT-Cy5 membranes show no increase in FRET signals over time (*SI Appendix*, Fig. S5 *E–H*) and dilution of WT-Cy5 samples with unlabeled protein does not change the photobleaching probability distribution over the course of a month (*SI Appendix*, Fig. S5*D*). This indicates that the dimers do not dissociate on the timescale investigated, which could occur for multiple reasons. One possibility for this observation is that an artifact is introduced during the membrane preparation exclusively in the WT samples. For example, consider the possibility of the freeze/thawing step generating two-dimensional crystals of the WT construct, but not N43S. If this were the case, then preformed WT-Cy3 and WT-Cy5 membranes would exist in larger crystalline assemblies that could protect dimers from dissociating. If these assemblies do not interact with each other, they would not exhibit a significant initial FRET signal or an increase in FRET over time. Crystalline assemblies have been observed for many reconstituted proteins at high densities (34, 35), suggesting this as a possibility. However, our FRET measurements of WT-Cy3/Cy5 provide data that do not support this hypothesis, as we would expect these samples to show an increase in FRET signal after freeze/thaw yet this is not the case (*SI Appendix*, Fig. S5*F*). We can also speculate about other possibilities, such as freeze/thaw shifting the isolated WT dimers into other conformations that prevent dissociation. However, Fluc is a small membrane protein with only four transmembrane helices, is entirely membrane embedded with minimal extramembrane loops. Any conformational change must reconcile fluoride permeation and Na^+ binding to the dimer, which we assume requires a precise structural arrangement. As N43S and WT are functionally similar when Na^+ is bound, this suggests that they are also structurally similar, but this emphasizes the need for future structural studies to investigate this fully.

Finally, we consider the hypothesis that the model system of N43S reflects a general assembly mechanism of Fluc, where WT exhibits altered reaction parameters that significantly shift the population to the active dimer with no practical observation of dissociation. *SI Appendix*, Fig. S7 depicts the model reaction involving two steps: (I) the monomer (M) assembling into the pseudo-stable dimer intermediate (D), followed by (II) Na^+ binding to the dimer intermediate to yield the conductive dimer form (D*). This is a linked equilibrium reaction, and as such, the apparent dimer population (D and D*) depends on the kinetics and thermodynamics associated with both reactions. The observation that WT Fluc only exists in the Na^+ bound D* state could arise in many ways, such as an increase in the stability of D vs. M, and/or increasing the affinity of Na^+ binding alone, thus increasing the observation of D*. Indeed, if WT follows a similar assembly reaction to N43S, but is effectively locked into the dimer state due to an increase in Na^+ binding, then this makes a clear prediction. If Na^+ can be removed from the WT protein, then it is expected that the protein would participate in a monomer–dimer equilibrium like what we observe with N43S. Then, addition of Na^+ would trap the protein in the active dimeric form, with no dynamic dissociation. To our knowledge, the only impactful removal of Na^+ from WT Fluc has been during exchange dialysis with Li^+ at higher temperatures, where the Na^+ exchange was incomplete and not fully reversible (18). While further work is needed to establish improved conditions, these results set the stage for future studies that may connect the model reaction that we observe for N43S to the WT form of the protein.

In summary, we found that a mutant form of the dimeric fluoride channel Fluc-Bpe, N43S, assembles via a dynamic equilibrium reaction of pseudo-stable monomers, driven initially by membrane-dependent forces. Because the monomers introduce a membrane defect in the dissociated state, subunits that find each other in the correct orientation in the membrane can associate prior to the formation of a protein–protein interface. Na^+ binding to this encounter complex then brings the protein into its functional dimeric state. The stabilization of the functional, conductive channel is dependent on Na^+ binding, that only offers weak stabilization of the dimer complex. For WT Fluc in which Na^+ binding affinity is presumed to be stronger, the dimer is long-lived and always in the conductive state. But simply weakening the backbone interactions around this site with N43S, reveals an underlying dynamic and thermodynamically driven reaction. These results map out the fundamentals of ion channel assembly, demonstrating that dynamic complexes can form and can be locked into conformational states with further ion and potential protein interactions. Thus, this study lays down the foundation for a general hypothesis for how ion channels assemble, disassemble, and are susceptible to regulation in biological membranes.

Materials and Methods

Fluc Constructs. Fluc-Bpe bearing two functionally neutral mutations, R29K and E94S, was introduced into a pASK vector encoding a C-terminal LysC recognition site and hexahistidine tag (TRKAASLVPRGSGGHHHHHH). All mutations were made by Quickchange II Site-Directed Mutagenesis (Agilent, Santa Clara #200523) followed by DNA sequencing of the full gene. We introduced two labeling sites, R29C and R128C. The N43S mutation was on the background of the R29K and E94S mutation. The molecular weights for each construct are 15,404 g/mol and they have an extinction coefficient $\varepsilon_{Fluc} = 39{,}380\ M^{-1}\ cm^{-1}$. Molecular weights and extinction coefficient were calculated using the Peptide Property Calculator (http://biotools.nubic.northwestern.edu/proteincalc.html).

Protein Purification. Expression and purification of Fluc-Bpe was carried out as previously described. C41 *E. coli* competent cells (Lucigen, #60442-1) were transformed with the plasmid and then 2 L Terrific Broth supplemented with ampicillin was inoculated and grown at 37 °C. Protein expression was induced with IPTG at OD600 = 1.0. After 1.5 h of induction, cells were harvested, then lysed by sonication in buffer supplemented with 5 mM reducing agent TCEP [Tris(2-carboxyethyl)phosphine] (Soltec Ventures, #M115) and pH adjusted to 7.5. Protein extraction was carried out with 2% n-Decyl-β-D-Maltopyranoside (DM; Anatrace #D322S25GM) for 2 h at room temperature. Cell debris was pelleted down, and the supernatant was run on a 2-mL column volume (CV) TALON cobalt affinity resin (Takara Bio #635504) equilibrated in CoWB/TCEP (100 mM NaCl (Sigma-Aldrich 746398), 20 mM Tris (RPI #1005479), 1 mM TCEP,

pH 7.5 with NaOH, 5 mM DM). After binding, the column was washed with 15 CVs of CoWB/TCEP followed by a low imidazole wash of CoWB/TCEP containing 40 mM imidazole (RPI #I52000). Fluc was eluted with CoWB/TCEP containing 400 mM imidazole, then concentrated in a 10 kDa NMWL centrifugal filters (Amicon #UFC9003) to ~500 μL and injected on a Superdex 200 10/30 GL size exclusion column (GE Healthcare #28990944) equilibrated in size exclusion buffer [SEB, 150 mM NaCl, 10 mM HEPES (Fisher Scientific # BP310-1), 10 mM NaF (Sigma-Aldrich #201154) pH 7, 5 mM analytical-grade DM (Anatrace #D32225GM)], attached to a medium pressure chromatography system (NGC, Bio-Rad). Protein fractions were collected, and the protein concentration was calculated from the absorbance at 280 nm (A_{280}) using a Nanodrop 2000c UV–VIS spectrophotometer (Thermo Scientific).

Labeling of Purified Protein. Cyanine3 (Cy3)-maleimide and Cyanine5 (Cy5)-maleimide dye was obtained as lyophilized powder as 50 mg (Lumiprobe #21080 #23080), stored as 10 mM master stocks (50 μL each) in anhydrous Dimethyl sulfoxide (Sigma–Aldrich #276855) at –80 °C. The fluorophore conjugation reaction was carried out in SEB with 10 μM Fluc subunits and 50 μM Cy3-maleimide, Cy5-maleimide, or a 1:8 mixture of both for 15 min at room temperature in dark. At the end of the reaction, 100-fold molar excess of cysteine (RPI #1004738) was added to quench the maleimide reaction, from freshly prepared 100 mM stock in CoWB, pH adjusted to 7.5. The "free" dye was separated from the labeled protein by binding the reaction mixture to a 250 μL cobalt affinity resin column equilibrated with 15 CV CoWB (no TCEP) in a Micro-Bio spin chromatography column (Bio-Rad Laboratories # 7326204), washed 15 CV with CoWB and then eluted with 400 mM imidazole in CoWB, manually collecting only the fluorescently labeled protein. To remove the interfering absorbance of imidazole at 280 nm, the labeled protein was added to a 3 mL Sephadex G50 size exclusion column (Cytiva #GE17-0042-01) equilibrated in CoWB (no TCEP). The fluorescently labeled protein was eluted after addition 2 to 2.5 mL of CoWB to the column. The concentration and labeling efficiency of protein calculated from the UV-VIS absorbance spectrum of the sample and λ_{max} of Fluc (280 nm), Cy3 (552 nm), and Cy5 (655 nm) as follows:

$$[Fluc_{Fluor}] = \frac{A_{280} - (A_{dye} \bullet CF)}{\varepsilon_{Fluc} \bullet l}, \quad [\mathbf{1}]$$

where l is the pathlength of 1 cm, ε_{Fluc} is the extinction coefficient, 39,380 M^{-1} cm^{-1}, A_{dye} is the peak absorbance of the dye (A_{Cy3} = 552 nm, A_{Cy5} = 655 nm), and CF is the correction factor of the dye absorbance at 280 nm (CF_{Cy3} = 0.08, CF_{Cy5} = 0.05).

$$P_{Fluor} = \frac{A_{dye}}{[Fluc_{Fluor}] \bullet \varepsilon_{dye} \bullet l}, \quad [\mathbf{2}]$$

where $\varepsilon_{dye}$is the extinction coefficient of the dye (ε_{Cy3} = 1.5 × 10^5 M^{-1} cm^{-1}; ε_{Cy5} = 2.5 × 10^5 M^{-1} cm^{-1}). Note, for the co-labeled sample, the concentration is calculated using the sum of $A_{Cy3} \times CF_{Cy3}$ and $A_{Cy5} \times CF_{Cy5}$. The acceptor to donor labeling ratio is calculated as P_{Cy5}/P_{Cy3}.

Lipid Preparation and Protein Reconstitution. Reconstitution of Fluc was carried out as described previously (14). Briefly, 25 mg/mL chloroform stocks of EPLs (Avanti Polar Lipids Inc. #100600C) were dried by evaporation under a stream of nitrogen gas until a thin dried film of lipids appeared. The film was washed with pentane (Sigma-Aldrich #236705-1L). Then, lipids were resolubilized in the required dialysis buffer with 35 mM CHAPS (Anatrace #C316S) for a final concentration of 20 mg/mL lipids. The lipid-detergent mixture was solubilized using a cup-horn sonicator (Qsonica, Newtown, CT) until the sample was transparent. Protein was added to the solubilized lipid-detergent mixture and placed into 3,500 MWCO dialysis cassettes (Thermo Scientific #66330), and then the samples were then dialyzed in the dark at room temperature in 1,000× sample volume with 4 buffer changes every 4 to 12 h. At the end of dialysis, the samples were freeze-thawed to form large paucilamellar vesicles. This involved 3 repetitions of freezing the samples at –80 °C and thawed in a room-temperature water bath. Samples were stored at room temperature, in the dark for the desired amount of time or frozen at –80 °C until used.

Fluoride Transport assay. The fluoride flux assay was performed as described previously (14, 36). Here, liposomes containing 300 mM fluoride are placed in a low-fluoride solution. Fluoride efflux is initiated by addition of valinomycin (Sigma-Aldrich #V0627) and monitored using a fluoride-selective electrode. After the fluoride efflux reaches a steady state, liposomes are disrupted by the addition of n-octyl-beta-D-glucoside (β-OG, Anatrace #O31125GM) to release the remaining encapsulated fluoride. The change in fluoride concentration over time normalized to the total fluoride concentration in the sample Δf_T can be fitted using Eq. **3** adapted from ref. 25.

$$\frac{\Delta f(t)}{\Delta f_T} = (1 - F_0)\left(1 - e^{-(k_{Fluc} + k_{leak})x}\right) + F_0\left(1 - e^{-k_{leak}x}\right). \quad [\mathbf{3}]$$

in which F_0 is the fraction of liposomes that does not contain active protein and k_{Fluc} and k_{leak} are the rate constants for F^- flux through the channel and for the background leak through the liposome membrane, respectively. For WT Fluc however, transport rates exceed the response time of the electrode. Therefore, the volume fractions of liposomes with no functional protein ($F_{0,\,vol}$) are calculated by subtracting the plateau value after addition of β-OG from the plateau value after addition of valinomycin.

Planar Lipid Bilayer Recordings. Single-channel recordings were performed as described previously via a Nanion Orbit-mini planar bilayer system, using 70% 1-palmitoyl-2-oleoyl-phosphatidylethanolamine, 30% 1-palmitoyl-2-oleoyl-phosphatidylglycerol (Avanti Polar Lipids #850757 & #840457), 5 mg/mL in n-nonane (Alfa Aesar #A16177-AE) to form bilayers. Single channels were inserted by addition of protein reconstituted liposomes to the "cis" side of the bilayer, and current was recorded at –200 mV holding potential (cis side defined as zero voltage) in symmetrical solutions containing 300 mM NaF, 10 mM NMG-Cl (Sigma-Aldrich #66930), 10 mM HEPES pH 7.0. Recordings were low-pass filtered at 160 Hz, digitized at 1.25 kHz, and analyzed in AXON Clampfit 10 (Molecular Devices Inc.). Channel conductance was measured from the difference between open vs. blocked current in each recording. All recordings shown in figures are representative of behavior seen on many channels in multiple reconstitutions.

To calculate the dwell time distributions of open and closed channels, we consider a bimolecular binding scheme with rate constants of Na^+ binding association k_{on} and dissociation k_{off}:

$$C + Na^+ \underset{k_{off}}{\overset{k_{on}}{\rightleftharpoons}} O_{Na^+}, \quad [\mathbf{4}]$$

$$\frac{1}{\tau_c} = k_{on}[Na^+], \quad [\mathbf{5}]$$

$$\frac{1}{\tau_o} = k_{off}, \quad [\mathbf{6}]$$

where O_{Na+}represents the Na^+ bound open channel.

Subunit Exchange Assay via Bulk FRET. These studies are based on the methodology outlined in ref. 9. The protein is labeled with either a donor- (Cy3-maleimide) or acceptor- (Cy5-maleimide) fluorophore or co-labeled with a mixture of both (in a 1:5 ratio of Cy3 to Cy5) and reconstituted into EPL membranes at 0.5 μg/mg. Donor- and acceptor-labeled proteoliposomes are then mixed matching the measured co-labeled ratio and fused together using repeated freezing and thawing (F/T) cycles. FRET is measured in a fluorometer (FL3-22, Horiba) by exciting Cy3 at 534 nm, measuring the emission intensity, I_{Cy3}, at 552 nm and I_{Cy5}, at 655 nm and calculating the ratiometric FRET as follows:

$$FRET\ \ Signal = \frac{I_{Cy5}}{I_{Cy3} + I_{Cy5}}. \quad [\mathbf{7}]$$

Single-Molecule TIRF (Total Internal Reflection Fluorescence) Microscopy. Photobleaching experiments were carried out as described previously (8). Imaging was performed on an objective-based TIRF microscope, setup for the imaging of single molecules. After loading the custom build slide onto the microscope, 30 μL of sample was loaded onto the lane and the flow cell was washed multiple times with dialysis buffer to remove any excess proteoliposomes not bound to the glass. The number of spots corresponding to proteoliposomes with labeled proteins was kept at a low density, less than 300 spots in the imaging

field, by diluting the samples with dialysis buffer if needed. The total number of spots imaged for each measurement was at least 300 spots. Before imaging, the sample was passed through a 0.4 μm polycarbonate membrane (Whatman) using a LiposoFast-Basic (Avestin) extruder.

Photobleaching Data Analysis and Dimerization K_D Estimation. The analysis of the photobleaching traces was carried out as described previously. Image files were analyzed using a MATLAB-based CoSMoS analysis program (37). Fluorescent spots were automatically selected by the image analysis software on the criteria of intensity and further selected via criteria (i.e., spots that were overlapping or at the edge of the field were excluded). Selected spots selected were analyzed using a 4 × 4 pixel area of interest (AOI) centered around the peak. The total pixel intensity within each AOI was integrated as a function of time, and then the intensity traces were examined for step-like decreases in intensity indicating irreversible photobleaching of fluorophores. The probabilities of single (P_1), double (P_2), and three or more steps (P_{3+}) were calculated. For fitting, we followed a fitting protocol that has been developed by the lab and is described in detail elsewhere (23). The experimentally obtained photobleaching distributions were fitted to modeled photobleaching distributions using least-squared analysis by performing iterative fitting of P_1, P_2, P_{3+} vs. $\chi_{reconstituted}$ photobleaching data while varying P_{fluor} and P_{bg} for estimating the labeling yield via the WT Fluc dimer or varying K_D for stability estimations. The resulting *Normalized SSR*$^{-1}$ is a probability distribution over the parameter space, where areas of higher probability are in better agreement with the experimental data than areas of lower probability. Using this distribution, we were able to infer an optimal point estimate as well as to quantify the uncertainty of all model parameters (23).

MD Simulations of Fluc in the Monomer, Dimer, and Dissociated Dimer States. The CG simulations reported in this study used two lipid bilayers of identical composition but different dimensions, prepared using insane.py (38) and represented by the MARTINI 2.2 forcefield (39). Both bilayers are mixtures of POPE and POPG lipids, in a 3:1 ratio, initially immersed in a 150 mM NaCl solution. The smaller system is approximately 10.0 × 10.0 × 8.7 nm in size, and comprises 336 lipids, 3,378 water particles, and 118 and 34 Na^+ and Cl^- ions, respectively; the larger system is approximately 20.2 × 20.2 × 9.6 nm, and comprises 676 lipids, 16,380 water particles, and 536 and 198 Na^+ and Cl^- ions, respectively. To equilibrate each of these systems, we carried out an MD simulation of 50 μs at 1 atm and 303 K, using GROMACS 2018.8 (40). After verifying equilibration (system size, lipid mixing, etc.), the smaller bilayer was used to examine the membrane morphology associated with monomeric and dimeric Fluc; the larger bilayer was used to simulate the self-assembly of dissociated dimers.

CG models of monomeric and dimeric Fluc were based on Protein Data Bank entry 5NKQ and were constructed with a customized version of martinize.py (38). For the monomeric form, both the WT and the N43S mutant were examined. Elastic networks to sustain the secondary and tertiary structures of the protein were created using lower and upper cut-off distances of 0.5 and 0.9 nm, respectively, a force constant of 500 kJ mol^{-1} nm^{-2}, and default values for the elastic-bond decay factor and decay power (-es 0 -ep 0). Glu88 was set as protonated due to its proximity to a F^- ion in the experimental structure; all other ionizable residues were set at their default protonation state at pH 7. To simulate the monomer and dimer, the protein structures were embedded into the smaller POPE/POPG lipid bilayer, as captured in the last snapshot of the 50 μs trajectory used for equilibration. To do so, the protein structures were superposed on the bilayer at its center, and lipid, solvent, and ions within 0.3 nm from any protein particle were removed; the number of Na^+ and Cl^- ions was then adjusted to increase the ionic strength to 300 mM while preserving a total net charge of zero. Following a series of short MD simulations to equilibrate the protein–lipid interface, a trajectory of 50 μs was calculated for each system, analogous to that calculated for the pure POPE/POPG lipid bilayer. The data reported in Figs. 3 and 4 derives from these trajectories, analyzed using the MOSAICS suite (28).

The dissociated dimer was simulated in the larger bilayer. To create this simulation system, a monomer was first embedded in the center of the membrane using the same protocol described above for the smaller bilayer. Following equilibration, a second monomer was inserted in the same membrane, in four different locations and orientations, at least 5 nm away from the monomer at the center. After equilibration, each of the four systems was simulated for 30 μs. To minimize the influence of direct monomer–monomer interactions in the outcome of these simulations, while simultaneously limiting the extent to which the two monomers can drift apart, the standard energy function was supplemented with an additional potential-energy term acting on the minimum distance between the two monomers, or d_{min}; to calculate this distance during runtime, all backbone CG particles in the transmembrane region of each protein were considered (30 per monomer). Specifically, this potential energy term is $E' = 0.5 \times K \times (d - d_{min})^2$ if $d_{min} \leq 1.3$ nm or $d_{min} \geq 5.5$ nm with $K = 500$ kJ mol^{-1} nm^{-2}. Note that for any other value of d_{min} this additional term is inactive i.e., $E' = 0$. Calculations of d_{min}, E' and the associated atomic forces were carried out using PLUMED 2.2.5 (41).

Two additional MD simulations were carried out for monomeric Fluc, with the N43S mutation, using an all-atom representation of the protein and its environment, based on the CHARMM36m forcefield (42). These trajectories were calculated with NAMD (43), in the NPT ensemble at 298 K and 1 atm and with periodic boundary conditions. To construct plausible input configurations for these simulations, the two snapshots that best represent the average shape of the ester layers of the membrane in the CG simulations of the same construct were selected. Lipids and solvent molecules were "backmapped" to an all-atom representation (44) and the X-ray structure of the protein replaced its CG version. The resulting molecular systems contained 79,346 atoms. Each system was equilibrated through a staged protocol where structural restraints are gradually weakened over 200 ns of simulation time. A trajectory of 400 ns was then calculated in each case and used for analysis. In both simulations, long-range electrostatic interactions were computed using the PME method with a 1.0-Å grid spacing and sixth-order splines for mesh interpolation. Real-space interactions (van der Waals and short-range electrostatics) were cut off at 12 Å. The equations of motion were integrated in 2 fs time steps and all covalent bonds involving H atoms were constrained at their reference lengths.

Statistical Analysis. Statistical analysis in each required experiment was performed using either unpaired Student's *t* test (two-tailed distribution) or ANOVA test with GraphPad Prism version 9 (one-way ANOVA and Uncorrected Fisher's least significant difference test). Details of statistical analyses, including sample sizes and biological replications, are provided in the figure legends.

Data, Materials, and Software Availability. Source data are included as supporting information. Microscopy image files and MD trajectories are very large in size and exceed the file size limit on most repositories. However, these data are backed up and archived in our institution, and we can provide the files upon request.

ACKNOWLEDGMENTS. The Robertson lab is supported by the National Institute of General Medical Science (NIGMS), NIH R01GM120260, and Melanie Ernst by the Millipore Sigma Predoctoral Award and American Heart Association grant 23PRE1013841. Randy Stockbridge is supported by NIGMS, NIH grant R35GM128768. The Faraldo-Gómez laboratory is supported by the Intramural Research Intramural Research Program of the National Heart, Lung, and Blood Institute (NHLBI), NIH, and computational resources were provided by the NIH High-Performance Computing System, Biowulf. We thank Dr. Benjamin McIlwain for preliminary electrophysiology experiments for N43S Fluc, Dr. Nathan Bernhardt for his assistance with data analysis, Dr. Rahul Chadda for his guidance on the FRET studies, the Chanda lab and Dr. Paul H. Schlesinger for the Nanion setup, and the Robertson lab members for useful discussions.

Author affiliations: [a]Department of Biochemistry and Molecular Biophysics, Washington University School of Medicine, St. Louis, MO 63110; [b]Theoretical Molecular Biophysics Section, National Heart, Lung, and Blood Institute, NIH, Bethesda, MD 20894; and [c]Department of Molecular, Cellular, and Developmental Biology, University of Michigan, Ann Arbor, MI 48109

1. W. A. Catterall, Voltage-gated calcium channels. *Csh Perspect. Biol.* **3**, a003947 (2011).
2. O. B. Clarke, J. M. Gulbis, Protein dimerization and oligomerization in biology. *Adv. Exp. Med. Biol.* **747**, 122–136 (2012).
3. M. de L. Ruiz, R. L. Kraus, Voltage-gated sodium channels: Structure, function, pharmacology, and clinical indications. *J. Med. Chem.* **58**, 7093–7118 (2015).
4. A. Samanta, T. E. T. Hughes, V. Y. Moiseenkova-Bell, Membrane protein complexes: Structure and function. *Subcell Biochem.* **87**, 141–165 (2018).
5. A. M. O'Connell, R. E. Koeppe II, O. S. Andersen, Kinetics of gramicidin channel formation in lipid bilayers: Transmembrane monomer association. *Science* **250**, 1256–1259 (1990).

6. T. A. Harroun, W. T. Heller, T. M. Weiss, L. Yang, H. W. Huang, Experimental evidence for hydrophobic matching and membrane-mediated interactions in lipid bilayers containing gramicidin. *Biophys. J.* **76**, 937–945 (1999).
7. T. A. Harroun, W. T. Heller, T. M. Weiss, L. Yang, H. W. Huang, Theoretical analysis of hydrophobic matching and membrane-mediated interactions in lipid bilayers containing gramicidin. *Biophys. J.* **76**, 3176–3185 (1999).
8. R. Chadda *et al.*, The dimerization equilibrium of a ClC Cl−/H+ antiporter in lipid bilayers. *Elife* **5**, e17438 (2016).
9. R. Chadda, T. Lee, P. Sandal, R. Mahoney-Kruszka, J. L. Robertson, A thermodynamic analysis of CLC transporter dimerization in lipid bilayers. *Proc. Natl. Acad. Sci. U.S.A.* **120**, e2305100120 (2023).
10. R. Chadda *et al.*, Membrane transporter dimerization driven by differential lipid solvation energetics of dissociated and associated states. *Elife* **10**, e63288 (2021).
11. S. E. Tusk, N. J. Delalez, R. M. Berry, Subunit exchange in protein complexes. *J. Mol. Biol.* **430**, 4557–4579 (2018).
12. R. R. Breaker, New insight on the response of bacteria to fluoride. *Caries Res.* **46**, 78–81 (2012).
13. E. Adamek, K. Pawłowska-Góral, K. Bober, In vitro and in vivo effects of fluoride ions on enzyme activity. *Ann. Acad. Med. Stetin* **2**, 69–85 (2005).
14. R. B. Stockbridge, J. L. Robertson, L. Kolmakova-Partensky, C. Miller, A family of fluoride-specific ion channels with dual-topology architecture. *Elife* **2**, e01084 (2013).
15. R. B. Stockbridge *et al.*, Crystal structures of a double-barrelled fluoride ion channel. *Nature* **525**, 548–551 (2015).
16. B. C. McIlwain, S. Newstead, R. B. Stockbridge, Cork-in-bottle occlusion of fluoride ion channels by crystallization chaperones. *Structure* **26**, 635–639.e1 (2018).
17. B. C. McIlwain, R. Gundepudi, B. B. Koff, R. B. Stockbridge, The fluoride permeation pathway and anion recognition in Fluc family fluoride channels. *Elife* **10**, e69482 (2021).
18. B. C. McIlwain, K. Martin, E. A. Hayter, R. B. Stockbridge, An interfacial sodium ion is an essential structural feature of fluc family fluoride channels. *J. Mol. Biol.* **432**, 1098–1108 (2020).
19. S. Chakrapani, A. Auerbach, A speed limit for conformational change of an allosteric membrane protein. *Proc. Natl. Acad. Sci. U.S.A.* **102**, 87–92 (2005).
20. I. B. Levitan, L. K. Kaczmarek, "Membrane ion channels and ion currents" in *The Neuron: Cell and Molecular Biology, 4 edn* (Oxford University Press, New York, 2015), pp. 63–84.
21. L. Cliff, R. Chadda, J. L. Robertson, Occupancy distributions of membrane proteins in heterogeneous liposome populations. *Biochim. Biophys. Acta Biomembr.* **1862**, 183033 (2020).
22. M. Ernst, T. N. Ozturk, J. L. Robertson, A single-molecule method for measuring fluorophore labeling yields for the study of membrane protein oligomerization in membranes. *PLoS One* **18**, e0280693 (2023).
23. M. Ernst, T. N. Ozturk, J. L. Robertson, A single-molecule method for measuring fluorophore labeling yields for the study of membrane protein oligomerization in membranes. *PLoS One* **18**, e0280693 (2022).
24. J. Wyman, S. J. Gill, *Binding and Linkage Functional Chemistry of Biological Macromolecules*, A. Kelly, Ed. (University Science Books, 1990).
25. M. Walden *et al.*, Uncoupling and turnover in a Cl−/H+ exchange transporter. *J. Gen. Physiol.* **129**, 317–329 (2007).
26. R. Chadda, L. Cliff, M. Brimberry, J. L. Robertson, A model-free method for measuring dimerization free energies of CLC-ec1 in lipid bilayers. *J. Gen. Physiol.* **150**, 355–365 (2018).
27. W. Zhou *et al.*, Large-scale state-dependent membrane remodeling by a transporter protein. *Elife* **8**, e50576 (2019).
28. N. Bernhardt, J. D. Faraldo-Gómez, MOSAICS: A software suite for analysis of membrane structure and dynamics in simulated trajectories. *Biophys. J.* **122**, 2023–2040 (2022), 10.1016/j.bpj.2022.11.005.
29. M. Javanainen, H. Martinez-Seara, I. Vattulainen, Excessive aggregation of membrane proteins in the Martini model. *PLoS One* **12**, e0187936 (2017).
30. J. L. Baker *et al.*, Widespread genetic switches and toxicity resistance proteins for fluoride. *Science* **335**, 233–235 (2012).
31. S. Lansky *et al.*, A pentameric TRPV3 channel with a dilated pore. *Nature* **621**, 206–214 (2023).
32. N. B. Woodall, Y. Yin, J. U. Bowie, Dual-topology insertion of a dual-topology membrane protein. *Nat. Commun.* **6**, 8099 (2015).
33. C. Anselmi, K. M. Davies, J. D. Faraldo-Gómez, Mitochondrial ATP synthase dimers spontaneously associate due to a long-range membrane-induced force. *J. Gen. Physiol.* **150**, 763–770 (2018).
34. Y. Jiang *et al.*, Membrane-mediated protein interactions drive membrane protein organization. *Nat. Commun.* **13**, 7373 (2022).
35. D. Oesterhelt, W. Stoeckenius, RHodopsin-like protein from the purple membrane of *Halobacterium halobium*. *Nat. New Biol.* **233**, 149–152 (1971).
36. R. B. Stockbridge *et al.*, Fluoride resistance and transport by riboswitch-controlled CLC antiporters. *Proc. Natl. Acad. Sci. U.S.A.* **109**, 15289–15294 (2012).
37. L. J. Friedman, J. Gelles, Multi-wavelength single-molecule fluorescence analysis of transcription mechanisms. *Methods* **86**, 27–36 (2015).
38. T. A. Wassenaar, H. I. Ingólfsson, R. A. Böckmann, D. P. Tieleman, S. J. Marrink, Computational lipidomics with insane: A versatile tool for generating custom membranes for molecular simulations. *J. Chem. Theory Comput.* **11**, 2144–2155 (2015).
39. D. H. de Jong *et al.*, Improved parameters for the martini coarse-grained protein force field. *J. Chem. Theory Comput.* **9**, 687–697 (2013).
40. M. J. Abraham *et al.*, GROMACS: High performance molecular simulations through multi-level parallelism from laptops to supercomputers. *Softwarex* **1**, 19–25 (2015).
41. M. Bonomi *et al.*, PLUMED: A portable plugin for free-energy calculations with molecular dynamics. *Comput. Phys. Commun.* **180**, 1961–1972 (2009).
42. J. Huang *et al.*, CHARMM36m: An improved force field for folded and intrinsically disordered proteins. *Nat. Methods* **14**, 71–73 (2017).
43. J. C. Phillips *et al.*, Scalable molecular dynamics on CPU and GPU architectures with NAMD. *J. Chem. Phys.* **153**, 044130 (2020).
44. T. A. Wassenaar, K. Pluhackova, R. A. Böckmann, S. J. Marrink, D. P. Tieleman, Going backward: A flexible geometric approach to reverse transformation from coarse grained to atomistic models. *J. Chem. Theory Comput.* **10**, 676–690 (2014).